A phase field model for damage in elasto-viscoplastic materials

P. Shanthraj [a,b,*], L. Sharma [a,c], B. Svendsen [a,d], F. Roters [a], D. Raabe [a]

[a] *Max-Planck-Institut für Eisenforschung, Max-Planck-Straße 1, 40237 Düsseldorf, Germany*
[b] *AICES, RWTH Aachen University, Schinkelstraße 2, 52062 Aachen, Germany*
[c] *Department of Mechanical Engineering, Eindhoven University of Technology, P.O. Box 513, 5600 MB, Eindhoven, The Netherlands*
[d] *Material Mechanics, RWTH Aachen University, Schinkelstraße 2, 52062 Aachen, Germany*

Available online 21 May 2016

Abstract

A phase field method for brittle fracture is formulated for a finite strain elasto-viscoplastic material using a novel obstacle phase field energy model. The obstacle energy model results in a crack profile with compact support, and thus gives a physically realistic description of the material behaviour at the vicinity of the crack tip. The resulting variational inequality is discretised by a finite element method, and is efficiently solved using a reduced space NEWTON method. The solution accuracy and numerical performance of this method is compared with a conventional phase field energy model for brittle fracture through representative examples, and a significant reduction in the numerical solution cost is demonstrated.
© 2016 Elsevier B.V. All rights reserved.

Keywords: Phase field; Viscoplasticity; Fracture; Finite deformation

1. Introduction

The prediction of crack initiation and propagation in microstructures in relation to its myriad configurations is of critical importance in the design of heterogeneous materials [1–3]. Traditional methods to characterise material failure are expensive and slow as they rely heavily on experiments [4–6]. Alternatively, numerical simulations can be used to substitute this process through predictive frameworks incorporating accurate constitutive models of the anisotropic and non-linear material behaviour, frequently encountered in engineering applications prior to failure [7,8]. In the field of continuum damage mechanics, damage is described as an internal state variable of the material [9,10], and thermodynamic frameworks have been developed that can describe the evolution of the internal damage state in a general setting [11–13]. The recently developed micromorphic approach of Forest [14] provides a link between these thermomechanical field theories and existing gradient methods [15,16], where the relationship between the internal state variable and the non-local field variable is enforced in a weak sense.

---

* Corresponding author at: Max-Planck-Institut für Eisenforschung, Max-Planck-Straße 1, 40237 Düsseldorf, Germany. Tel.: +49 211 6792 825; fax: +49 211 6792 333.
E-mail address: p.shanthraj@mpie.de (P. Shanthraj).

In recent years, the phase field method (PFM) has emerged as a powerful and versatile tool to model brittle fracture and non-local damage processes [17–22]. This is almost certainly true from a multiphysics perspective, since, a phase field approach facilitates the modelling of any number of coupled chemical, thermal and deformation processes having an influence on the stored energy of the material [23]. The PFM for brittle fracture is based on the recently developed variational theory [24,25], which is an extension of the classical theory of GRIFFITH. However, with the notable exceptions of Borden et al. [21] and Miehe et al. [26], the application of these PFMs to the general case of a finite strain elasto-viscoplastic material has been relatively unexplored. Following the terminology of Cahn and Hilliard [27], the phase field energy of an interface is composed of a gradient and a homogeneous contribution. The conventional PFM for brittle fracture described in the above works use a quadratic model for the homogeneous contribution to the phase field energy with a minimum at the undamaged material state. The regularised crack profile resulting from the use of such an energy model decays exponentially away from the discrete crack surface, and thus does not have compact support [18]. This non-compactness manifests in a non-physical influence of the discrete crack surface on the constitutive response of a distant material point, and is especially pertinent for non-linear constitutive models, where a small change in the elastic degradation, due to a decaying damage profile, can result in significant changes in the constitutive response of a distant material point. The situation is exacerbated when studying crack nucleation phenomena, where the absence of localised stress concentrations at a pre-existing crack tip can result is an extremely diffused damage profile. In [16], a gradient damage model with a linear form of the homogeneous contribution to the phase field energy is analysed. The resulting regularised crack profile has a compact support, thus resulting in a physically desirable decoupling between the regularised crack profile and the constitutive response of a distant material point.

In the current work, a PFM for brittle fracture is formulated, extending the approach of Pham et al. [16] for elasto-viscoplastic materials undergoing large deformations. The linear model for the homogeneous phase field energy is augmented with an indicator function to enforce constraints on the evolution of the damage phase field resulting form physical considerations such as irreversibility and non-negativity, *i.e.* $0 \leq \varphi(t_n) \leq \varphi(t_{n-1})$. A reduced space NEWTON method [28] is then applied to efficiently solve the resulting variational inequality. This paper is organised as follows: the derivation of the constitutive models and field equations are presented in Section 2, followed by an outline of their numerical implementation in Section 3. In Section 4, representative examples are used to benchmark and compare the proposed method with a conventional PFM for brittle fracture. A summary is provided in Section 5 along with perspectives for future applications.

2. Theory

2.1. Kinematics

Let $\mathcal{B}_0 \subset \mathbb{R}^3$ be a microstructural domain of interest, with boundary $\partial \mathcal{B}_0$. The deformation resulting from an applied loading defines a field $\chi(\mathbf{x}) : \mathbf{x} \in \mathcal{B}_0 \to \mathbf{y} \in \mathcal{B}$ mapping points $\mathbf{x}$ in the reference configuration $\mathcal{B}_0$ to points $\mathbf{y}$ in the deformed configuration $\mathcal{B}$. The total deformation gradient, given by $\mathbf{F} = \partial \chi / \partial \mathbf{x} = \nabla \chi$, is multiplicatively decomposed into elastic and plastic components as $\mathbf{F} = \mathbf{F}_e \mathbf{F}_p$. An anisotropic elastic stiffness, $\mathbb{C}$, relates the elastic deformation gradient, $\mathbf{F}_e$ to the second PIOLA–KIRCHHOFF stress, $\mathbf{S} = \mathbb{C}(\mathbf{F}_e^T \mathbf{F}_e - \mathbf{I})/2$. The plastic velocity gradient, $\mathbf{L}_p = \dot{\mathbf{F}}_p \mathbf{F}_p^{-1}$, is driven by $\mathbf{S}$ by virtue of the chosen plasticity model.

2.2. Thermodynamics

Restricting attention to isothermal and quasi-static processes with no external heat supply, the balance laws for linear momentum, angular momentum, internal energy, and total entropy, given by Šilhavý [11, Chapter 3]

$$\mathbf{0} = \text{Div } \mathbf{P}, \qquad \mathbf{F}\mathbf{P}^T = \mathbf{F}^T\mathbf{P}, \qquad \dot{\varepsilon} = \mathbf{P} \cdot \dot{\mathbf{F}}, \qquad \dot{\eta} = \pi \tag{1}$$

where, $\mathbf{P}$ is the first PIOLA–KIRCHHOFF stress, ε is the internal energy density, η represents the entropy density, and π is the entropy production-rate density. Through the absolute temperature θ, the entropy balance (Eq. (1)$_4$) can be written in the corresponding dissipation balance form

$$\theta \dot{\eta} = \delta \tag{2}$$

where $\delta := \theta\pi$ represents the dissipation-rate density. Combination of Eqs. (1)$_3$ and (2) then yields the reduced form

$$\delta = \mathbf{P} \cdot \nabla\dot{\boldsymbol{\chi}} - \dot{\psi} \tag{3}$$

of the dissipation-rate density δ, again at constant temperature, where $\psi := \varepsilon - \theta\,\eta$ represents the free energy density.

All models for the free energy density to be discussed represent special cases of the general form

$$\psi = \psi\left(\nabla\boldsymbol{\chi}, \mathbf{F}_\mathrm{p}, \boldsymbol{\xi}, \varphi, \nabla\varphi\right) \tag{4}$$

for this energy in terms of the inelastic local deformation, $\mathbf{F}_\mathrm{p}$, a set, $\boldsymbol{\xi}$, of local internal variables, and the damage phase field, φ.

Modelling the stress as purely energetic, we have

$$\mathbf{P} = \partial_{\nabla\boldsymbol{\chi}}\psi \tag{5}$$

for the first PIOLA–KIRCHHOFF stress. In this case,

$$
\begin{aligned}
\int_{\mathcal{B}_0} \delta \; \mathrm{d}\mathbf{x} &= -\int_{\mathcal{B}_0}\left[\partial_\varphi\psi\,\dot{\varphi} + \partial_{\nabla\varphi}\psi\cdot\nabla\dot{\varphi} + \partial_{\mathbf{F}_\mathrm{p}}\psi\cdot\dot{\mathbf{F}}_\mathrm{p} + \partial_{\boldsymbol{\xi}}\psi\cdot\dot{\boldsymbol{\xi}}\right]\mathrm{d}\mathbf{x}\\
&= -\int_{\mathcal{B}_0}\left[\delta_\varphi\psi\,\dot{\varphi} + \partial_{\mathbf{F}_\mathrm{p}}\psi\cdot\dot{\mathbf{F}}_\mathrm{p} + \partial_{\boldsymbol{\xi}}\psi\cdot\dot{\boldsymbol{\xi}}\right]\mathrm{d}\mathbf{x} - \int_{\partial\mathcal{B}_0}\partial_{\nabla\varphi}\psi\cdot\mathbf{n}\,\dot{\varphi}\,\mathrm{d}\mathbf{s}
\end{aligned} \tag{6}
$$

follows from Eq. (4) for the dissipation rate with respect to $\mathcal{B}_0$, where

$$\delta_x f = \partial_x f - \mathrm{Div}\,\partial_{\nabla x} f \tag{7}$$

represents the variational derivative. Assuming no-flux (Neumann) or constant-rate (Dirichlet) boundary conditions, *i.e.*,

$$\partial_{\nabla\varphi}\psi\cdot\mathbf{n}|_{\partial\mathcal{B}_0} = 0, \quad \text{or} \quad \dot{\varphi}|_{\partial\mathcal{B}_0} = 0 \tag{8}$$

respectively, Eq. (6) reduces to the purely bulk form

$$\delta = -\delta_\varphi\psi\,\dot{\varphi} - \partial_{\mathbf{F}_\mathrm{p}}\psi\cdot\dot{\mathbf{F}}_\mathrm{p} - \partial_{\boldsymbol{\xi}}\psi\cdot\dot{\boldsymbol{\xi}} \tag{9}$$

for the dissipation rate and its density.

To model kinetics in the context of Eq. (9), attention is restricted here to constitutive relations based on the dissipation potential

$$\chi = \chi(\partial_{\mathbf{F}_\mathrm{p}}\psi, \partial_{\boldsymbol{\xi}}\psi, \delta_\varphi\psi). \tag{10}$$

By design, this potential determines the dependent constitutive quantities

$$\dot{\varphi} = -\partial_{\delta_\varphi\psi}\chi, \qquad \dot{\mathbf{F}}_\mathrm{p} = -\partial_{\partial_{\mathbf{F}_\mathrm{p}}\psi}\chi, \qquad \dot{\boldsymbol{\xi}} = -\partial_{\partial_{\boldsymbol{\xi}}\psi}\chi \tag{11}$$

and so the following residual form of the dissipation-rate density via Eq. (9)

$$\delta = \delta_\varphi\psi\,\partial_{\delta_\varphi\psi}\chi + \partial_{\mathbf{F}_\mathrm{p}}\psi\cdot\partial_{\partial_{\mathbf{F}_\mathrm{p}}\psi}\chi + \partial_{\boldsymbol{\xi}}\psi\cdot\partial_{\partial_{\boldsymbol{\xi}}\psi}\chi. \tag{12}$$

Assuming further that χ is non-negative and convex in the thermodynamic driving forces, *i.e.*,

$$\delta_\varphi\psi\,\partial_{\delta_\varphi\psi}\chi + \partial_{\mathbf{F}_\mathrm{p}}\psi\cdot\partial_{\partial_{\mathbf{F}_\mathrm{p}}\psi}\chi + \partial_{\boldsymbol{\xi}}\psi\cdot\partial_{\partial_{\boldsymbol{\xi}}\psi}\chi \geqslant \chi \geqslant 0 \tag{13}$$

the resultant constitutive form equation (12) is sufficient for fulfilment of the dissipation principle $\delta \geqslant 0$.

2.3. Constitutive modelling

Using the above general formalism, a constitutive law is now reduced to specifying two potentials: the free energy, ψ, and the dissipation potential, χ, along with a suitable parameterisation of the microstructure as a set of internal

state variables. In the current constitutive model, the total free energy is separated

$$\psi = \psi_E + \psi_D + \psi_P \tag{14}$$

into an elastic contribution, a damage contribution and a plastic contribution.

2.3.1. Brittle damage mechanics

In the current brittle damage constitutive model, the damage phase field variable, φ, is used to represent the elastic degradation between undamaged, *i.e.* $\varphi = 1$, and completely damaged, *i.e.* $\varphi = 0$, states. A simple form of the elastic free energy satisfying these requirements is given by,

$$\psi_E(\nabla\boldsymbol{\chi}, \mathbf{F}_p, \varphi) = \varphi^2 \, \tilde{\psi}_E(\nabla\boldsymbol{\chi}, \mathbf{F}_p) \tag{15}$$

where, $\tilde{\psi}_E$ is the stored elastic energy density in the undamaged state.

The damage contribution to the free energy is given by the phase field approximation of the energy of a discrete crack surface, and is composed of a gradient contribution and a homogeneous contribution

$$\psi_D(\nabla\varphi, \varphi) = \psi_{G0} \, |\nabla\varphi|^2 + \psi_{H0}(1 - \varphi)^m + I_{[0,1]}(\varphi) \tag{16}$$

where ψ_{G0} and ψ_{H0} are material constants, and m is the order of the phase field potential. The quadratic model for the homogeneous contribution to the phase field energy, used in conventional PFMs for brittle fracture [17–19,21], is recovered by setting $m = 2$, and the linear model of Pham et al. [16] is obtained by setting $m = 1$. The indicator function on the interval [0, 1], defined such that $I_{[0,1]}(\varphi)$ vanishes for $\varphi \in [0, 1]$ and $+\infty$ otherwise, is introduced to enforce physically reasonable bounds for the damage phase field, *i.e.* $0 \le \varphi \le 1$.

The thermodynamic driving forces conjugate to the phase field variable can be obtained from Eq. (9) as

$$\delta_\varphi \psi = 2\varphi \, \tilde{\psi}_E - m\psi_{H0}(1 - \varphi)^{m-1} - \text{Div } 2\psi_{G0}\nabla\varphi + \mu \tag{17}$$

where $\mu \in \partial I_{[0,1]}(\varphi)$ is the subdifferential of the indicator function. The constitutive description is completed by specifying the following convex, non-negative form of the dissipation potential,

$$\chi_D = \frac{1}{2} M \left(\delta_\varphi \psi\right)^2 \tag{18}$$

where M is a mobility parameter. Eq. (18) results in the following field equation for the evolution of φ

$$\dot{\varphi} = -M \left[2\varphi \, \tilde{\psi}_E - m\psi_{H0}(1 - \varphi)^{m-1} - \text{Div } 2\psi_{G0}\nabla\varphi + \mu \right]. \tag{19}$$

2.3.2. Phenomenological crystal plasticity

The crystal plasticity model used in the present study (for details see [29]), is an adoption of the phenomenological description of Peirce et al. [30] for face-centred cubic crystals. The plastic velocity gradient $\mathbf{L}_p$ is composed of the slip rates $\dot{\gamma}^\alpha$ on each of the 12 FCC $\{111\}\langle\bar{1}10\rangle$ slip systems, which are indexed by $\alpha = 1, \dots, 12$.

$$\mathbf{L}_p = \dot{\mathbf{F}}_p \mathbf{F}_p^{-1} = \sum_\alpha \dot{\gamma}^\alpha \, \mathbf{s}^\alpha \otimes \mathbf{n}^\alpha \tag{20}$$

where $\mathbf{s}^\alpha$ and $\mathbf{n}^\alpha$ are unit vectors along the slip direction and slip plane normal, respectively. The thermodynamic driving force conjugate to $\mathbf{F}_p$, given by

$$\partial_{\mathbf{F}_p} \psi = -\varphi^2 \, \mathbf{S} \, \mathbf{F}_p^{-T} \tag{21}$$

can then be reduced to the simpler slip system based conjugate pair

$$-\partial_{\mathbf{F}_p} \psi \cdot \dot{\mathbf{F}}_p = \sum_\alpha \partial_{\gamma^\alpha} \psi \, \dot{\gamma}^\alpha, \quad \text{where } \partial_{\gamma^\alpha} \psi = -\varphi^2 \, \mathbf{S} \cdot (\mathbf{s}^\alpha \otimes \mathbf{n}^\alpha) = -\tau^\alpha \tag{22}$$

the plasticity constitutive equations are given by

$$\dot{\gamma}^{\alpha} = \partial_{\tau^{\alpha}} \chi_{\mathrm{P}} = \dot{\gamma}_0 \left| \frac{\tau^{\alpha}}{g^{\alpha}} \right|^n \mathrm{sgn}\left(\tau^{\alpha}\right) \tag{23}$$

in terms of,

$$\chi_{\mathrm{P}} = \frac{1}{n+1} \sum_{\alpha} \dot{\gamma}_0 \left| \frac{\tau^{\alpha}}{g^{\alpha}} \right|^{n+1}. \tag{24}$$

The slip resistances on each slip system, g^{α}, evolve asymptotically towards g_{∞} with shear γ^{β} ($\beta = 1, \ldots, 12$) according to the relationship

$$\dot{g}^{\alpha} = \dot{\gamma}^{\beta} h_0 \left| 1 - g^{\beta}/g_{\infty} \right|^a \mathrm{sgn}\left(1 - g^{\beta}/g_{\infty}\right) h_{\alpha\beta} \tag{25}$$

with parameters h_0 and a. The interaction between different slip systems is captured by the hardening matrix $h_{\alpha\beta}$.

2.4. Interface energy scaling

The energy coefficients $\psi_{\mathrm{H}0}$ and $\psi_{\mathrm{G}0}$ in the phase field energy in Eq. (16) can be related to the interface energy, g_0, by following the general approach of Cahn and Hilliard [27] for an infinite 1D domain, where

$$g_0 = \int_{-\infty}^{\infty} \psi(x) \, dx. \tag{26}$$

Neglecting elastic contributions, the free energy density, ψ, consists of a homogeneous and gradient contribution

$$\psi(x) = \psi_{\mathrm{H}}(\varphi(x)) + \psi_{\mathrm{G}}(\partial_x \varphi(x)), \qquad \psi_{\mathrm{G}}(\partial_x \varphi) = \psi_{\mathrm{G}0} \left| \partial_x \varphi \right|^2 \tag{27}$$

where $\psi_{\mathrm{G}0}$ is a material constant. Together with the boundary conditions $\varphi(\pm\infty) = \phi_{\pm}$ and $\partial_x \varphi(-\infty) = 0$, we have at equilibrium

$$\delta_{\varphi} \psi = 0 \implies \partial_{\varphi} \psi_{\mathrm{H}} = \partial_x \partial_{\partial_x \varphi} \psi_{\mathrm{G}} = \partial_x \{2 \, \psi_{\mathrm{G}0} \, \partial_x \varphi\} = 2 \, \psi_{\mathrm{G}0} \, \partial_x \partial_x \varphi. \tag{28}$$

Multiplying both sides by $\partial_x \varphi$ and integrating yields

$$\int_{-\infty}^{x} 2 \, \psi_{\mathrm{G}0} \, \partial_{\xi} \partial_{\xi} \varphi \, \partial_{\xi} \varphi \, d\xi = \int_{-\infty}^{x} \partial_{\xi} \psi_{\mathrm{G}}(\partial_x \varphi(\xi)) \, d\xi = \psi_{\mathrm{G}}(\partial_x \varphi(x)) \tag{29}$$

$$\int_{-\infty}^{x} \partial_{\varphi} \psi_{\mathrm{H}} \, \partial_{\xi} \varphi \, d\xi = \int_{-\infty}^{x} \partial_{\xi} \psi_{\mathrm{H}}(\varphi(\xi)) \, d\xi = \int_{\varphi_-}^{\varphi(x)} \partial_{\zeta} \psi_{\mathrm{H}}(\zeta) \, d\zeta = \Delta \psi_{\mathrm{H}}(\varphi(x)) \tag{30}$$

where $\Delta \psi_{\mathrm{H}}(\varphi(x)) = \psi_{\mathrm{H}}(\varphi(x)) - \psi_{\mathrm{H}}(\varphi_-)$. For $\psi_{\mathrm{G}}(\partial_x \varphi(x))$ in equilibrium

$$|\partial_x \varphi| = \sqrt{\frac{\Delta \psi_{\mathrm{H}}(\varphi)}{\psi_{\mathrm{G}0}}}, \quad \text{and} \quad \psi = \psi_{\mathrm{H}} + \Delta \psi_{\mathrm{H}} \tag{31}$$

then follows for the equilibrium form of $\partial_x \varphi$ and ψ. Using Eq. (31), to obtain the following change of variables

$$dx = \frac{1}{\partial_x \varphi} \, d\varphi = \mathrm{sgn}(\partial_x \varphi) \sqrt{\frac{\psi_{\mathrm{G}0}}{\Delta \psi_{\mathrm{H}}(\varphi)}} \, d\varphi \tag{32}$$

the integral in Eq. (26) can be evaluated to yield the following relation between $\psi_{\mathrm{G}0}$ and g_0

$$g_0 = \kappa_{\mathrm{H}0} \sqrt{\psi_{\mathrm{G}0}}, \quad \kappa_{\mathrm{H}0} = \mathrm{sgn}(\partial_x \varphi) \int_{\varphi_-}^{\varphi_+} \frac{\psi_{\mathrm{H}}(\varphi) + \Delta \psi_{\mathrm{H}}(\varphi)}{\sqrt{\Delta \psi_{\mathrm{H}}(\varphi)}} d\varphi. \tag{33}$$

Assuming that the midpoint of the regularised crack surface is at $x = 0$. Let $l_0 \geqslant 0$ represent the interface width in the sense that $\varphi(\pm l_0/2) \approx \varphi_\pm$. The Taylor-series expansion $\varphi(x) = \varphi(0) + \partial_x\varphi(0)\,x + \frac{1}{2}\partial_x^2\varphi(0)\,x^2 + \cdots$ then implies

$$\varphi_+ - \varphi_- = \partial_x\varphi(0)\,l_0 - \tfrac{1}{24}\partial_x^3\varphi(0)\,l_0^3 + \cdots \approx \partial_x\varphi(0)\,l_0 \tag{34}$$

in the case of a flat interface. Since $l_0 \geqslant 0$ by definition,

$$l_0 = \frac{|\varphi_+ - \varphi_-|}{|\partial_x\varphi(0)|}, \qquad \mathrm{sgn}(\partial_x\varphi(0)) = \mathrm{sgn}(\varphi_+ - \varphi_-). \tag{35}$$

Given Eq. (35), Eq. (31) implies the connection

$$l_0 = \kappa_{G0}\sqrt{\psi_{G0}}, \quad \kappa_{G0} = \frac{|\varphi_+ - \varphi_-|}{\sqrt{\Delta\psi_H(\varphi_0)}}, \tag{36}$$

between ψ_{G0} and l_0, with $\varphi_0 = \varphi(0)$. Combination of Eqs. (33) and (36) then implies the result for ψ_{G0}

$$\psi_{G0} = \frac{g_0 l_0}{\kappa_{H0}\kappa_{G0}}. \tag{37}$$

Considering the scaled form of the homogeneous energy, $\psi_H(\varphi) = \psi_{H0}\,\varphi_H(\varphi)$, with ψ_{H0} constant and $\varphi_H(\varphi)$ dimensionless, Eqs. (33) and (36) yields

$$\psi_{H0} = \frac{c_{G0}}{c_{H0}}\frac{g_0}{l_0}, \qquad \psi_{G0} = \frac{1}{c_{H0}c_{G0}}\,g_0 l_0 \tag{38}$$

where

$$c_{H0} := \mathrm{sgn}(\varphi_+ - \varphi_-)\int_{\varphi_-}^{\varphi_+} \frac{\varphi_H(\varphi) + \Delta\varphi_H(\varphi)}{\sqrt{\Delta\varphi_H(\varphi)}}\,d\varphi, \qquad c_{G0} := \frac{|\varphi_+ - \varphi_-|}{\sqrt{\Delta\varphi_H(\varphi_0)}}. \tag{39}$$

The resulting scaled form of the free energy density, in terms of the interface energy g_0 and interface width l_0, is given by

$$\psi_H(\varphi) = \frac{c_{G0}}{c_{H0}}\frac{g_0}{l_0}\,\varphi_H(\varphi), \qquad \psi_G(\partial_x\varphi) = \frac{1}{c_{H0}c_{G0}}\,g_0 l_0\,|\partial_x\varphi|^2. \tag{40}$$

In particular, the form of the homogeneous energy used in Eq. (16), *i.e.* $\varphi_H = (1 - \varphi)^m$, yields $c_{H0} = \frac{4}{m+2}$ and $c_{G0} = \sqrt{2m}$. In the simplest case of ideal brittle failure, the vanishing of l_0 corresponds to classic GRIFFITH failure [17,16].

3. Numerical implementation

The constitutive model introduced in Section 2.3 is implemented within the material simulation kit, DAMASK [31], and a large-scale parallel finite element (FE) code using the PETSc numerical library [32], is developed to handle the discretisation and numerical solution of the coupled field equations.

3.1. Finite element implementation

The starting point for the FE implementation of the field equations $(1)_1$ and (19) is their weak forms, given by

$$\mathbf{0} = \int_{\mathcal{B}_0} \nabla\delta\boldsymbol{\chi} \cdot \mathbf{P}\,\mathrm{d}\mathbf{x} \tag{41}$$

$$0 \leq \int_{\mathcal{B}_0} \left[(\delta\varphi - \varphi)\left(\frac{\dot\varphi}{M} + 2\varphi\,\tilde\psi_E - m\psi_{H0}(1 - \varphi)^{m-1}\right) - \nabla(\delta\varphi - \varphi)\cdot 2\psi_{G0}\nabla\varphi \right]\mathrm{d}\mathbf{x} \tag{42}$$

where $\delta\boldsymbol{\chi}$ and $\delta\varphi$ are the virtual deformation and damage phase fields respectively, such that $0 \leq \delta\varphi \leq 1$. No-flux (Neumann) boundary conditions are assumed for the sake of simplicity. Note that the evolution of the phase field variable, given in its strong form by Eq. (19), is formulated here in its weak form as a variational inequality.

The deformation field, $\boldsymbol{\chi}(\mathbf{x})$, and damage phase field, $\varphi(\mathbf{x})$, in addition to their virtual counterparts $\delta\boldsymbol{\chi}(\mathbf{x})$ and $\delta\varphi(\mathbf{x})$ are discretised as $\tilde{\boldsymbol{\chi}}(\mathbf{x})$, $\tilde{\varphi}(\mathbf{x})$, $\tilde{\delta\boldsymbol{\chi}}(\mathbf{x})$ and $\tilde{\delta\varphi}(\mathbf{x})$ respectively, using FE shape functions

$$\tilde{\boldsymbol{\chi}}(\mathbf{x}) = \sum_i N_i^{\chi}(\mathbf{x})\tilde{\boldsymbol{\chi}}_i, \quad \text{and} \quad \tilde{\varphi}(\mathbf{x}) = \sum_i N_i^{\varphi}(\mathbf{x})\tilde{\varphi}_i \tag{43}$$

$$\tilde{\delta\boldsymbol{\chi}}(\mathbf{x}) = \sum_i N_i^{\chi}(\mathbf{x})\delta\tilde{\boldsymbol{\chi}}_i, \quad \text{and} \quad \tilde{\delta\varphi}(\mathbf{x}) = \sum_i N_i^{\varphi}(\mathbf{x})\delta\tilde{\varphi}_i \tag{44}$$

where, $\tilde{\boldsymbol{\chi}}_i, \tilde{\varphi}_i, \delta\tilde{\boldsymbol{\chi}}_i$, and $\delta\tilde{\varphi}_i$ are the degrees of freedom of the respective discretised field. N_i^{χ} and N_i^{φ} are the FE shape functions, and the corresponding discrete differential operator matrices are $\mathbf{B}_i^{\chi}$ and $\mathbf{B}_i^{\varphi}$. Under these approximations, the weak form equations (41) and (42) can be rewritten as

$$\mathcal{R}_{\text{mech}} := \sum_i \delta\tilde{\boldsymbol{\chi}}_i^T \int_{\mathcal{B}_0} ([\mathbf{B}_i^{\chi}]^T)\tilde{\mathbf{P}}d\mathcal{B}_0 = \mathbf{0} \tag{45}$$

and

$$\mathcal{R}_{\text{dam}} := \sum_i [\tilde{\delta\varphi} - \tilde{\varphi}]_i^T \int_{\mathcal{B}_0} [N_i^{\varphi}]^T \left[\frac{N_i^{\varphi}\tilde{\varphi}_i}{M} + 2\tilde{\psi}_{\text{E}}N_i^{\varphi}\tilde{\varphi}_i - m\psi_{\text{H0}}N_i^{\varphi}[\mathbf{1} - \tilde{\varphi}_i]^{m-1} \right] d\mathbf{x}$$
$$- \sum_i [\tilde{\delta\varphi} - \tilde{\varphi}]_i^T \int_{\mathcal{B}_0} [\mathbf{B}_i^{\varphi}]^T 2\psi_{\text{G0}}\mathbf{B}_i^{\varphi}\tilde{\varphi}_i \, d\mathbf{x} \geq 0 \tag{46}$$

which defines a non-linear system of constrained equations for the unknowns $([\tilde{\boldsymbol{\chi}}]_i, [\tilde{\varphi}]_i)$. A time-discrete system of equations is obtained by using a backward EULER approximation

$$\dot{\tilde{\varphi}} = \frac{\tilde{\varphi}(t_n) - \tilde{\varphi}(t_{n-1})}{\Delta t} \tag{47}$$

of the rate $\dot{\tilde{\varphi}}$ in Eq. (46). Furthermore, irreversibility of the damage process can be enforced in the time discrete setting by restricting the trial space in the variational inequality such that $0 \leq \delta\tilde{\varphi} \leq \tilde{\varphi}(t_{n-1})$.

3.2. Numerical solution

The solution approach followed in this work involves solving the block lower triangular form of the coupled system of equations (45) and (46) within a staggered iterative loop until a self consistent solution is achieved for a time increment. The procedure is detailed in Algorithm 1. Through such a staggered approach, the solution scheme of each field can be described independently.

The mechanical equilibrium equation (45) is solved using an inexact NEWTON method with a critical point secant line search [33]. Within each NEWTON iteration, a flexible GMRES linear solver [34] preconditioned with a smoothed-aggregation algebraic multigrid method [35] is used for the linear solve.

The variation inequality (46) for the evolution of the phase field variable is solved using reduced space NEWTON method [28]. In this approach, the phase field system is partitioned into sets composed of degrees of freedom on which the upper and lower bound constraints are active, respectively $\mathcal{A}_+$ and $\mathcal{A}_-$, given by

$$\mathcal{A}_+(t_n) = \left\{ i \,|\, \tilde{\varphi}_i(t_n) \geq \tilde{\varphi}_i(t_{n-1}) \text{ and } \mathcal{R}_{\text{dam},i} \leq 0 \right\} \tag{48}$$

$$\mathcal{A}_-(t_n) = \left\{ i \,|\, \tilde{\varphi}_i(t_n) \leq 0 \text{ and } \mathcal{R}_{\text{dam},i} \geq 0 \right\} \tag{49}$$

and their complement, the inactive set, $\mathcal{I}$, composed of the phase field degrees of freedom on which the upper and lower bound constraints are inactive. Within each NEWTON iteration, a reduced system consisting the degrees of freedom belonging to the inactive set is solved using direct factorisation. It is important to note here that the size of the inactive set, $\mathcal{I}$, is expected to be significantly larger when using a quadratic energy model compared to a linear

energy model for the homogeneous contribution to the phase field energy in Eq. (16), since the quadratic energy model crack profile has non-compact support.

Algorithm 1: Staggered algorithm for field solution in $[t_{n-1}, t_n]$.

Data: $[\chi]_{t_{n-1}}, [\varphi]_{t_{n-1}}$
Result: $[\chi]_{t_n}, [\varphi]_{t_n}$

1 Initialisation:

$[\varphi]_{t_n}^0 = [\varphi]_{t_{n-1}}$,

$[\chi]_{t_n}^0 = [\chi]_{t_{n-1}}$,

Impose boundary conditions in the vectors: $[\chi]_{t_n}^1$, $[\varphi]_{t_n}^1$

$j = 1$

2 **while** $\| [\varphi]_{t_n}^j - [\varphi]_{t_n}^{j-1} \|_2 \geq tol_\varphi$ *and* $\| [\chi]_{t_n}^j - [\chi]_{t_n}^{j-1} \|_2 \geq tol_\chi$ **do**

3 $\quad$ solve $R_{mech}([\chi]_{t_n}^j, [\varphi]_{t_n}^{j-1}) = 0$ for $[\chi]_{t_n}^j$;

4 $\quad$ solve $R_{dam}([\chi]_{t_n}^j, [\varphi]_{t_n}^j) = 0$ for $[\varphi]_{t_n}^j$;

5 $\quad$ $j = j+1$

6 **end**

7

$[\varphi]_{t_n} = [\varphi]_{t_n}^j$,

$[\chi]_{t_n} = [\chi]_{t_n}^j$

---

4. Results and discussion

4.1. Notch tension test

A square plate of length 1 mm, containing a horizontal notch of length 0.25 mm and tip radius 0.05 mm, is subjected to uniaxial tension strain of 0.02% by prescribing a vertical displacement on the top and bottom boundaries. The geometry and boundary conditions used are illustrated in Fig. 1a. An isotropic elastic material model is used with elastic constants, $C_{11} = 168.0$ GPa and $C_{12} = 121.4$ GPa, interface energy, $g_0 = 2.5$ J m^{-2}, and interface width, $l_0 = 25$ μm. The plate is meshed using simplex elements, and to study the effect of element size, three different meshes having element sizes 2 μm, 5 μm and 10 μm respectively are considered.

The load–displacement curves are shown in Fig. 2. For the linear energy model, global unloading is observed to initiate at a displacement of 0.12 μm, and the unloading behaviour is similar for the range of element sizes considered. The load–displacement curve resulting from the use of a linear and quadratic energy model for the intermediate mesh is also compared in Fig. 2. While global unloading is observed to initiate at the same displacement in both cases, a sharper transition from damaged to un-damaged states is observed in the case of the linear model. The damage phase field for the mode I crack resulting from the linear and quadratic energy model is shown in Fig. 3. It can be observed that the quadratic energy model damage phase field is diffused compared to the linear energy model damage phase field, which has a compact support. The damage phase field profile along a section through the crack is shown in Fig. 4. A crack half-width of around 50 μm, *i.e.* $2l_0$, is observed for all the meshes considered. The crack profile resulting from the linear energy model is observed to increase rapidly to the undamaged state, *i.e.* $\varphi = 1$, whereas the crack profile resulting from the quadratic energy model is observed to be more diffuse.

The evolution of the total, bulk and surface energies for the different element sizes are shown in Fig. 5. It is seen that, initially, the total energy is composed primarily of the bulk elastic energy, which increases quadratically with displacement as expected for a linear elastic material. At the critical point, at a displacement of 0.12 μm, a dissipation of the elastic energy resulting from the material unloading due to crack propagation is observed accompanied by a sharp increase in the surface energy contribution from the resulting crack surface. When the material is fully fractured,
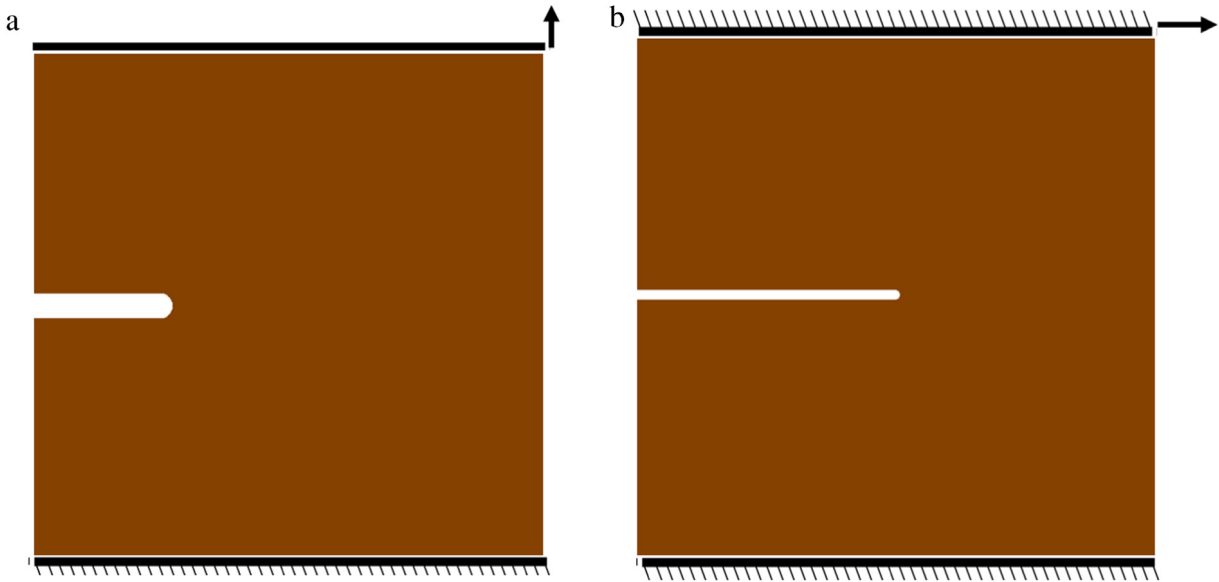
Fig. 1. Two-dimensional elastic plate with edge notch subjected to (a) uniaxial tension and (b) simple shear loading conditions.
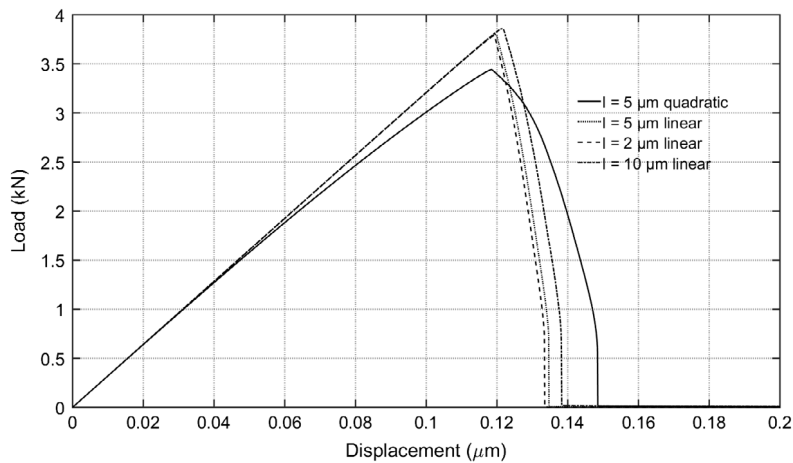

Fig. 2. Load–displacement curves for a notched elastic plate subjected to uniaxial tension.

the surface energy reaches a steady state value corresponding to the surface energy of the full crack, while the elastic bulk energy is fully dissipated. The resulting surface energy of the crack is overestimated in the coarser meshes for both linear and quadratic energy models, and converges to the theoretically predicted value of around 187.5 μJ, *i.e.* $g_0 l_c$ for a final crack length $l_c = 0.75$ mm, for the fine mesh. It is also noted that the resulting fracture energy is higher than that of the theoretically predicted value in both linear and quadratic case, with the deviation being larger in the quadratic model. An overestimation of the fracture energy is expected, and can be overcome through the use of a back-tracking solution algorithm [36].

In order to compare the numerical performance of the two energy models, the number of staggered iterations required for Algorithm 1 to converge is plotted as a function of the loading in Fig. 6. During the unloading period, the linear energy model requires between 6 and 9 staggered iterations for each load increment to converge, compared to between 4 and 9 iterations required by the quadratic energy model. However, due to the sharp transition between undamaged and fully damaged states, the linear model results in a more numerically efficient method overall, with a total of 3037 staggered iterations required compared with 3321 iteration required by the quadratic model.
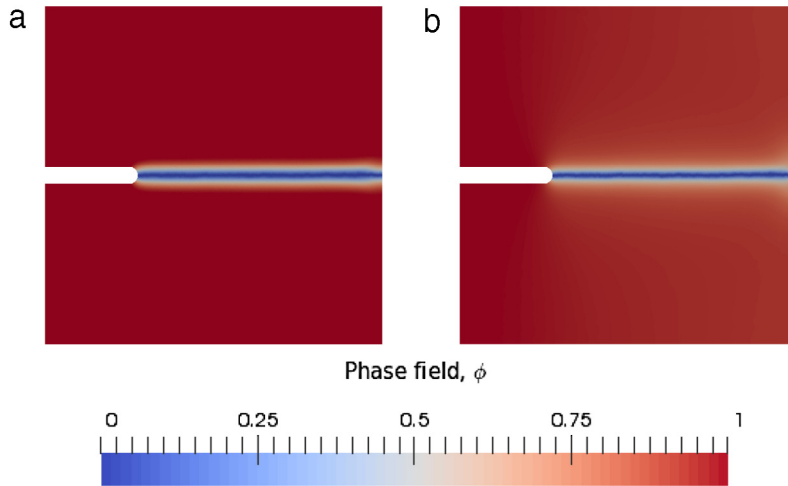
Fig. 3. The damage phase field in a notched elastic plate subjected to uniaxial tension using (a) a linear energy model and (b) a quadratic energy model.
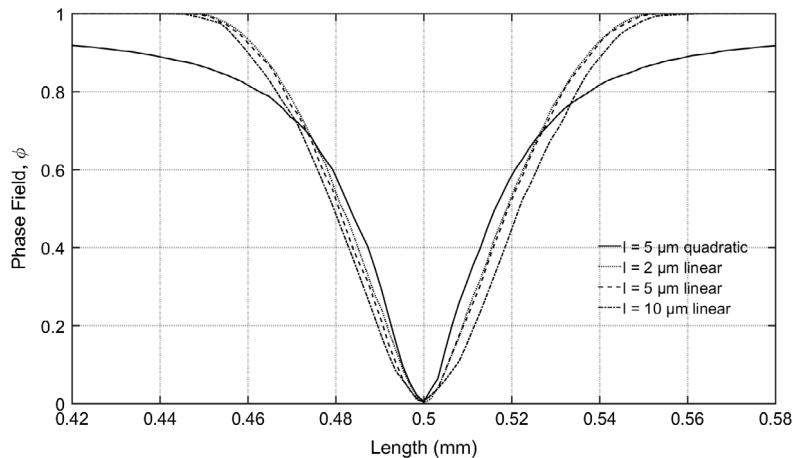

Fig. 4. The damage phase field profile across the crack in a notched elastic plate subjected to uniaxial tension.

4.2. Notch shear test

A square plate of length 1 mm, containing a horizontal notch of length 0.5 mm and tip radius 0.01 mm, is subjected to a simple shear strain of 0.025% by prescribing a horizontal displacement on the top and bottom boundaries, while fixing the vertical displacements. The geometry and boundary conditions used are illustrated in Fig. 1b. An isotropic elastic material model is used with elastic constants, $C_{11} = 168.0$ GPa and $C_{12} = 121.4$ GPa, interface energy, $g_0 = 2.5$ J m^{-2}, and interface width, $l_0 = 20$ μm. The plate is meshed using simplex elements, with an element size of 5 μm.

The load–displacement curves are shown in Fig. 7. In both the linear and quadratic energy models, global unloading is observed to initiate at a displacement of 0.17 μm. Similar to the tensile case, a sharper transition from damaged to un-damaged states is observed in the linear case compared to the quadratic energy model. The resulting crack patterns are shown in Fig. 8. In order to account for damage only in tension, the elastic energy is split into tensile and compressive components, with damage only affecting the tensile component [17,18,37,22]. The notch shear test has been extensively used as a benchmark in the PFM literature [18,22], and the crack pattern resulting from the linear energy model compares favourably with these works. Furthermore, it is observed that the resulting damage profile is compactly supported around the crack surface. On the other hand, the crack pattern resulting from the quadratic energy
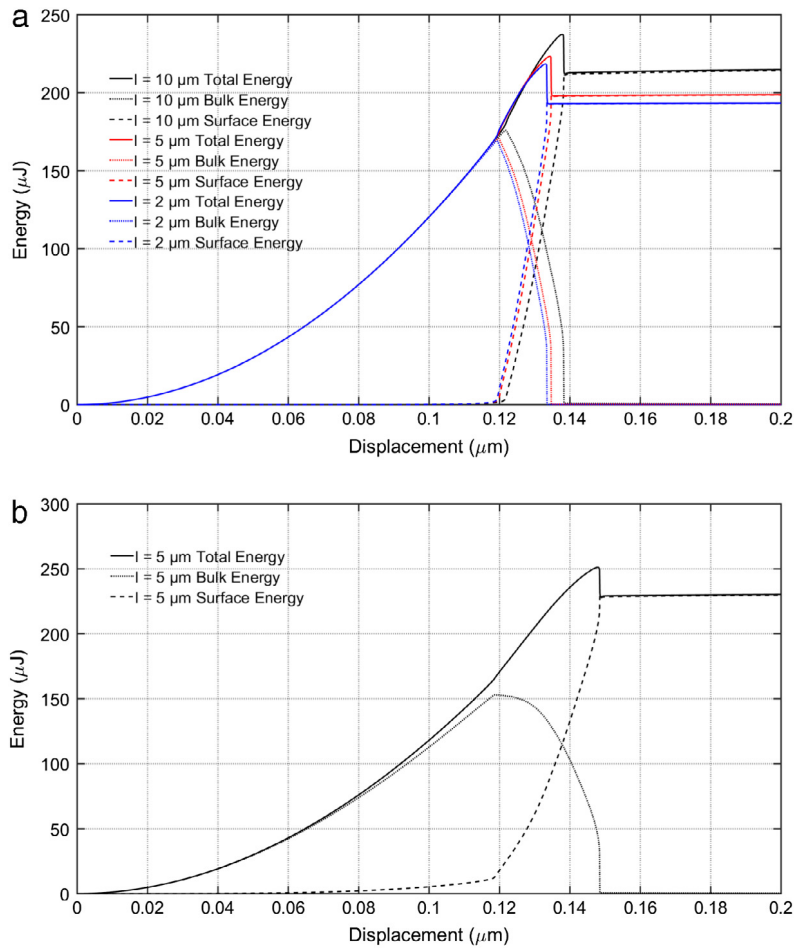
Fig. 5. The evolution of the total, bulk and surface energies during mode I cracking of a notched elastic plate using (a) a linear energy model and (b) a quadratic energy model.
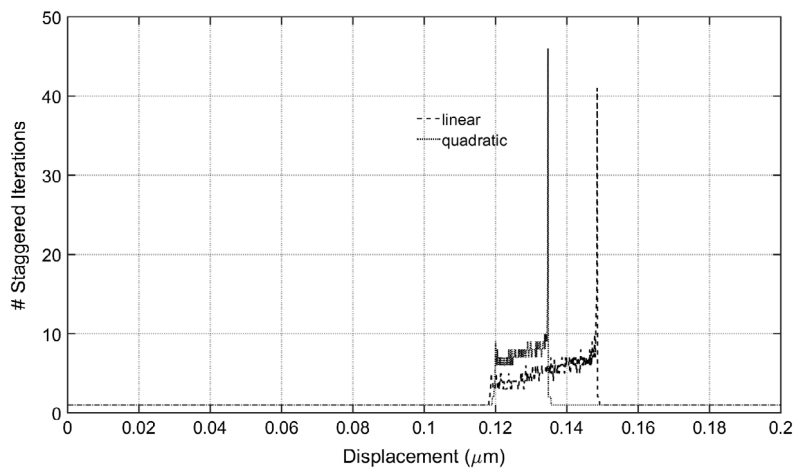

Fig. 6. Load–displacement curves for a notched elastic plate subjected to simple shear.

model exhibits a significantly diffused damage profile, which results in spurious damage evolution at the specimen corners due to the long range interaction between the phase field and the material response.
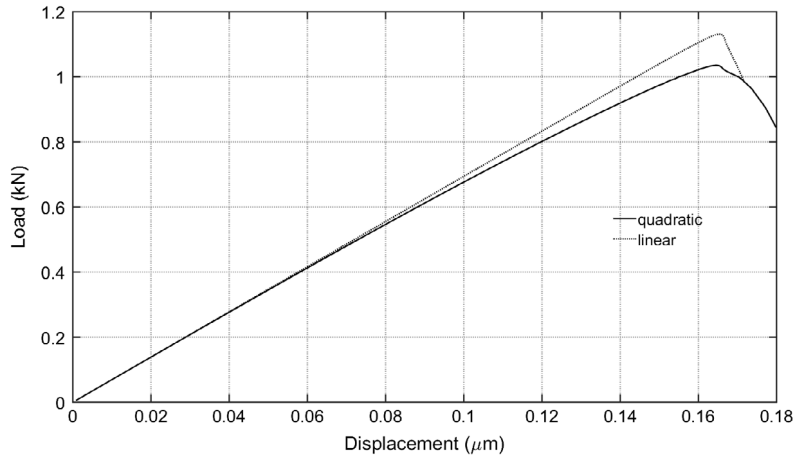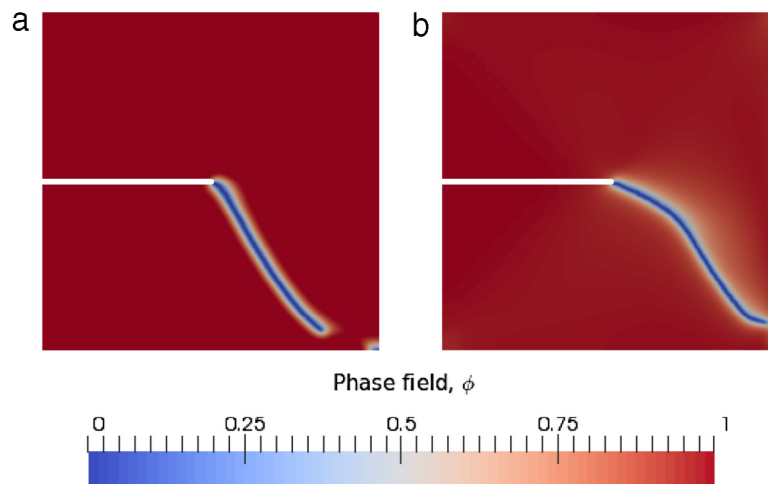
Fig. 7. Load–displacement curves for a notched elastic plate subjected to simple shear.

Fig. 8. The damage phase field in a notched elastic plate subjected to simple shear tension using (a) a linear energy model and (b) a quadratic energy model.

4.3. Polycrystal

To study crack nucleation phenomena in more complex engineering materials, the developed PFM is applied to study the deformation and failure of a plastically deforming polycrystalline material. The polycrystalline patch used, shown in Fig. 9, was generated by a VORONOI tessellation of 30 seed points randomly distributed within a square domain of length 1 mm, and the orientations of the individual grains were assigned randomly. A uniform simplex mesh of the polycrystalline patch was then generated, resulting in a uniform mesh with an average element size of 1.5 µm. LAGRANGE P2 and P1 elements were used to discretise the deformation and damage phase fields respectively. The patch is loaded through a displacement boundary condition applied in the horizontal direction at a nominal strain rate of $0.01 \ \mathrm{s}^{-1}$, up to a final time of 2 s, in 200 uniform increments. A phenomenological crystal plasticity constitutive model is used, and the material parameters are listed in Table 1.

The results obtained using a linear energy model are compared with the results obtained using a conventional quadratic energy model. Fig. 10 shows the evolution of the linear energy model damage phase field at different stages of the fracture process. It is again observed that the resulting profile of the regularised crack surface is compact. Fig. 11 shows the evolution of the quadratic energy model damage phase field. The non-compact character of the crack profile is exacerbated by the absence of a strong stress concentration at a pre-existing crack tip during nucleation.
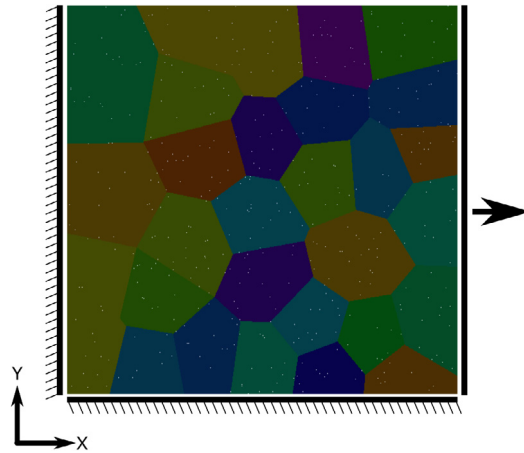
Fig. 9. Polycrystalline patch generated from a VORONOI tessellation of 30 randomly distributed seed points. Each colour represents a randomly assigned crystallographic orientation. (For interpretation of the references to colour in this figure legend, the reader is referred to the web version of this article.)
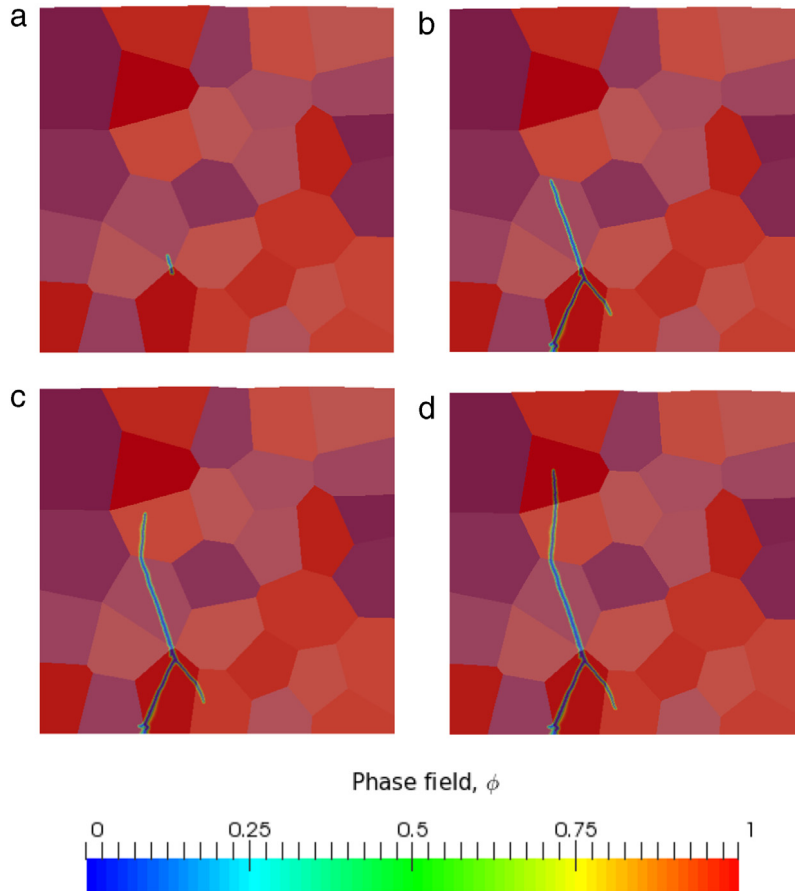

Fig. 10. Linear energy model: Evolution of the damage phase field in a polycrystalline patch loaded with a nominal strain rate of 0.01 s^{-1} at (a) 1.21 s, (b) 1.41 s, (c) 1.51 s and (d) 1.61 s.

The resulting normal component of the stress tensor in the loading direction for the linear and quadratic energy models are shown in Figs. 12 and 13 respectively. Differences are observed in the linear and quadratic energy model
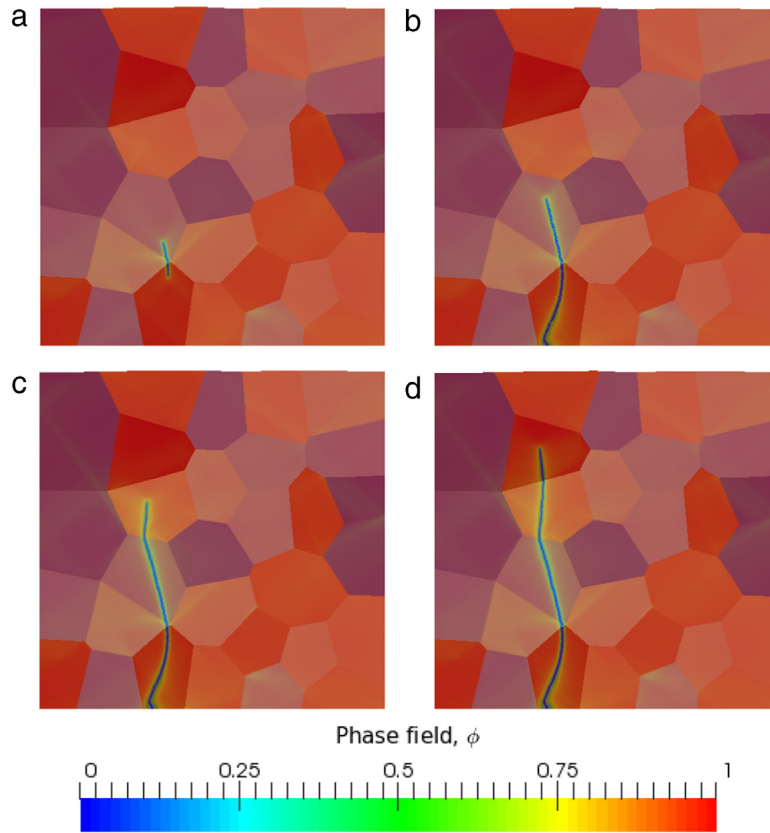
Fig. 11. Quadratic energy model: Evolution of the damage phase field in a polycrystalline patch loaded with a nominal strain rate of 0.01 s^{-1} at (a) 1.16 s, (b) 1.21 s, (c) 1.26 s and (d) 1.31 s.

Table 1
Material parameters: elastic constants C_{ab}, reference shear rate $\dot{\gamma}_0$, stress exponent n, initial and saturation flowstress s_0 (or τ_0) and s_∞ (or τ_∞), hardening parameters h_0, $h_{\alpha\beta}$, and a, interface energy, g_0, characteristic length, l_0, and damage mobility, M.

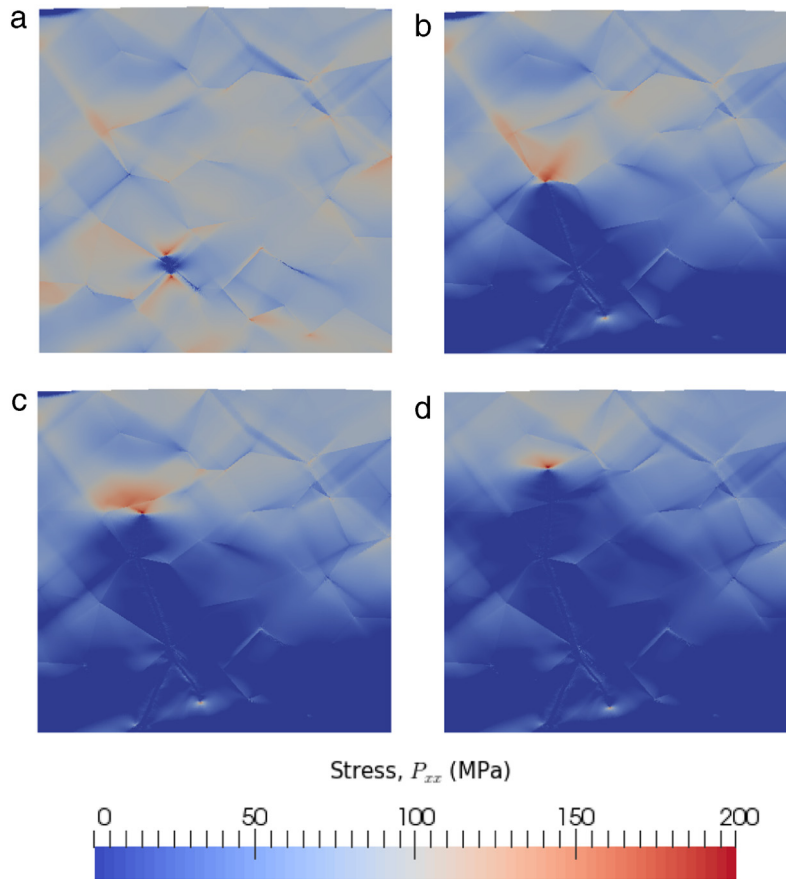| Parameter	Unit	Value
C_{11}	GPa	168.0
C_{12}	GPa	121.4
C_{44}	GPa	28.34
$\dot{\gamma}_0$	s^{-1}	1e−3
n		20
g_0	MPa	31
g_∞	MPa	63
a		2.25
h_0	MPa	75
Coplanar $h_{\alpha\beta}$		1
Non-coplanar $h_{\alpha\beta}$		1.4
g_0	J m^{-2}	1.0
l_0	μm	1.5
M	s^{-1}	0.01

Fig. 12. Linear energy model: Evolution of the horizontal normal stress component in a polycrystalline patch loaded with a nominal strain rate of 0.01 s^{-1} at (a) 1.21 s, (b) 1.41 s, (c) 1.51 s and (d) 1.61 s.

stress field distributions in the vicinity of the crack tip, which is attributed to the differences in the corresponding crack profiles. In a plastically deforming material, where small differences in the stresses can result in markedly different material response, such a spurious long range influence of the quadratic energy model stress field can be significant. Crack branching is observed following nucleation in the evolution of the linear energy model damage phase field, which is absent in the evolution of the quadratic energy model damage phase field, and is attributed to the differences in resulting stress fields and damage profiles during crack nucleation.

The crack nucleation is observed at a quadruple grain boundary junction in both cases. Crack nucleation at high order grain boundary junctions occurs due to the incompatibility of the plastic deformation modes in the respective grains forming the junction, which results in large stresses. Crack nucleation and its subsequent evolution during deformation strongly depends on the texture of the material due to the anisotropy of the plastic deformation modes, and highlights the need for accurate constitutive models. The nucleation and growth of a crack is followed by an unloading of the material behind the crack tips and a general redistribution of the stress field. The propagation of a nucleated crack is determined by the energetics of the material surrounding the crack tip. The crack tip stress field, and hence the elastic energy release rate is maximum in the direction of the crack, which results in a strong driving force for the propagation of the crack in this direction. However, the crack propagation path in engineering materials is rarely straight at the microstructural scale, and a significant amount of crack kinking is predicted by the model, due to the heterogeneity of the stress field in the neighbourhood of the crack tip. Crack kinking is observed towards regions of stress concentrations in neighbouring grain boundary junctions. The global stress response and its subsequent unloading at a stress of around 110 MPa is shown in Fig. 14. A slight difference in the global yielding behaviour of the material prior to crack nucleation is observed, which is attributed to the differences in the linear and quadratic
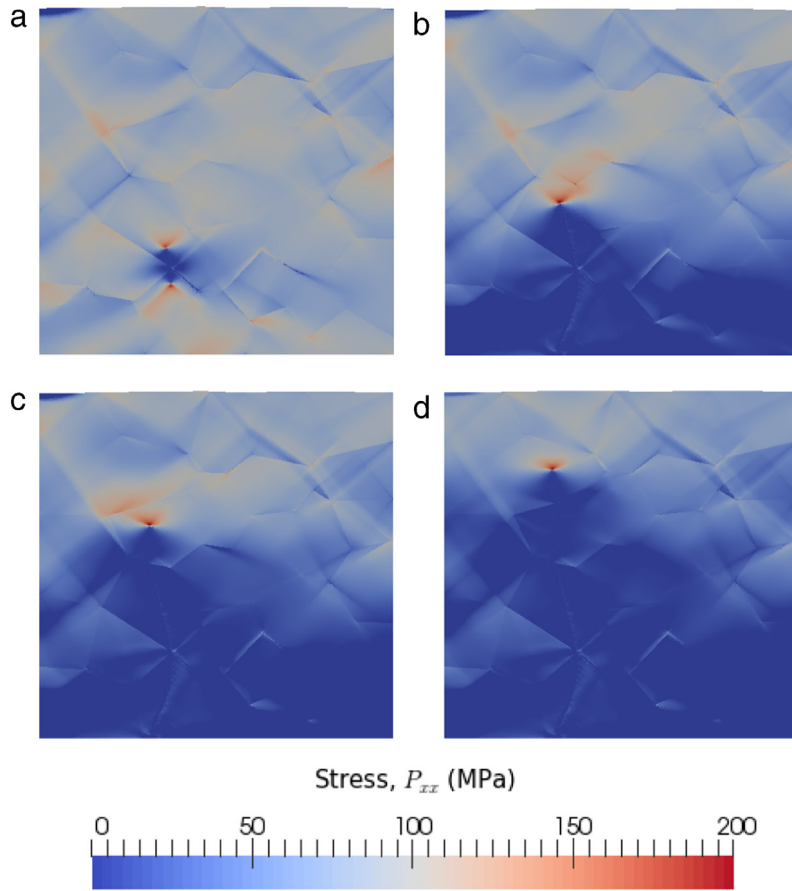
Fig. 13. Quadratic energy model: Evolution of the horizontal normal stress component in a polycrystalline patch loaded with a nominal strain rate of 0.01 s^{-1} at (a) 1.16 s, (b) 1.21 s, (c) 1.26 s and (d) 1.31 s.
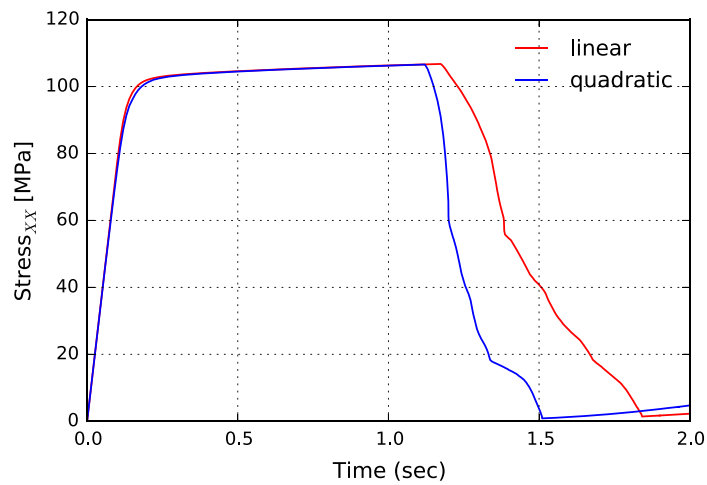

Fig. 14. Global stress response of the polycrystalline patch with linear and quadratic energy models.

energy model damage profiles, *i.e.* the linear energy model damage profile is fixed at the upper bound, while the quadratic energy model damage profile evolves prior to crack nucleation.
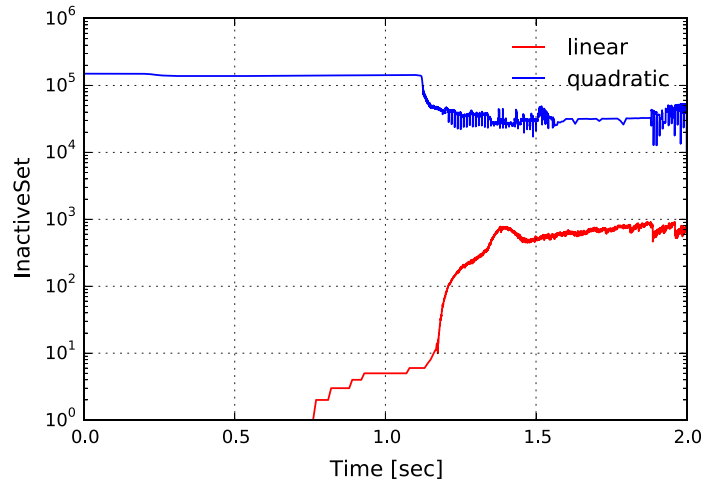
Fig. 15. Evolution of the inactive set size during the deformation and fracture of the polycrystalline patch with linear and quadratic energy models.

The evolution of the size of the inactive set resulting from the constraints the damage phase field (Section 3) is shown in Fig. 15. The size of the inactive set determines the system size of the phase field equations to be solved and is a good indicator of the numerical cost of the method. The inactive set resulting from the linear energy model is empty prior to crack nucleation as all the phase field degrees of freedom are fixed at the upper bound, while the inactive set resulting from the quadratic energy model is full prior to crack nucleation. Subsequent to crack nucleation, the increase in the linear energy model inactive set size corresponds to the degrees of freedom along the growing crack interface, while the decrease in the quadratic energy model inactive set corresponds to the degrees of freedom inside a fully damaged region, where the lower bound constraint is active. During crack propagation, a difference in the inactive set size of more than two orders of magnitude in observed, which translates to significant reduction in numerical cost of the linear energy model PFM compared with the quadratic energy model PFM.

5. Conclusions

In the current work, a PFM for brittle fracture is formulated for a finite strain elasto-viscoplastic material. In the approach followed, a novel obstacle phase field energy model is proposed, which results in a physically realistic description of the material behaviour in the vicinity of the crack tip. The resulting constraints on the evolution of the phase field variable is formulated as a variational inequality, and an efficient reduced space NEWTON method is used to solve the discretised system of equations. Coupling with mechanical equilibrium is performed in staggered iterations till a consistent solution is obtained.

Analytical scaling relations for the interface energy are established for the proposed energy model, and the resulting PFM is applied to investigate the finite-strain deformation and failure of a edge-notched and polycrystalline material. The resulting crack pattern in the edge-notched specimen under tension and simple shear loading is used to validate the method. The compact nature of the resulting damage profile is seen to alleviate boundary artefacts observed in a conventional PFM, and provides a more physically realistic representation of the crack tip. In the polycrystalline material, crack nucleation and propagation is critically dependent upon the anisotropic plastic response of the material and microstructural heterogeneity, with grain junctions serving as favourable sites. A reduction in the numerical cost of solving the phase field problem of more than two orders of magnitude is achieved for the proposed linear order PFM compared with a conventional quadratic order PFM. Additionally, a fewer number of iterations is required for convergence of the staggered scheme, thus reducing the overall numerical cost, which is dominated by the mechanical problem. The proposed method is capable of predicting complex crack patterns resulting from a rich set of interrelated driving forces, typically observed in the failure of engineering materials.

Appendix. Notation

As a general scheme of notation, vectors are written as boldface lowercase letters (*e.g.* $\mathbf{a}$, $\mathbf{b}$), second-order tensors as boldface capital letters (*e.g.* $\mathbf{A}$, $\mathbf{B}$), and fourth-order tensors as blackboard-bold capital letters (*e.g.* $\mathbb{A}$, $\mathbb{B}$). For vectors and tensors, Cartesian components are denoted as, respectively, a_i, A_{ij} and A_{ijkl}. Second-order tensors are represented in this work as linear mappings between vectors and is denoted as $\mathbf{Ab}$ (in components $A_{ij}b_j$, implicit summation over repeated indices is used unless specified otherwise) and, likewise, fourth-order tensors represent linear mappings between second-order tensors and is designated as $\mathbb{A}\mathbf{B}$ ($A_{ijkl}B_{kl}$). The composition of two second-order tensors is denoted as $\mathbf{AB}$ ($A_{ik}B_{kj}$). The tensor (or dyadic) product between two vectors is denoted as $\mathbf{a} \otimes \mathbf{b}$ ($a_i b_j$). All inner products are indicated by a single dot between the tensorial quantities of the same order, *e.g.*, $\mathbf{a} \cdot \mathbf{b}$ ($a_i b_i$) for vectors and $\mathbf{A} \cdot \mathbf{B}$ ($A_{ij}B_{ij}$) for second-order tensors. The transpose, $\mathbf{A}^{\mathrm{T}}$, of a tensor $\mathbf{A}$ is denoted by a superscript "T", and the inverse, $\mathbf{A}^{-1}$, by a superscript "−1". Additional notation is introduced where required.

References

[1] O. Bouaziz, Y. Brechet, J. Embury, Heterogeneous and architectured materials: a possible strategy for design of structural materials, Adv. Energy Mater. 10 (1–2) (2008) 24–36.

[2] R.O. Ritchie, Mechanisms of fatigue-crack propagation in ductile and brittle solids, Int. J. Fract. 100 (1) (1999) 55–83.

[3] M. Koyama, C.C. Tasan, E. Akiyama, K. Tsuzaki, D. Raabe, Hydrogen-assisted decohesion and localized plasticity in dual-phase steel, Acta Mater. 70 (2014) 174–187.

[4] G. Requena, E. Maire, C. Leguen, S. Thuillier, Separation of nucleation and growth of voids during tensile deformation of a dual phase steel using synchrotron microtomography, Mater. Sci. Eng. A 589 (2014) 242–251.

[5] H. Toda, S. Yamamoto, M. Kobayashi, K. Uesugi, H. Zhang, Direct measurement procedure for three-dimensional local crack driving force using synchrotron X-ray microtomography, Acta Mater. 56 (20) (2008) 6027–6039.

[6] H. Weiland, J. Nardiello, S. Zaefferer, S. Cheong, J. Papazian, D. Raabe, Microstructural aspects of crack nucleation during cyclic loading of AA7075-T651, Eng. Fract. Mech. 76 (5) (2009) 709–714.

[7] P. Shanthraj, M. Zikry, Microstructurally induced fracture nucleation and propagation in martensitic steels, J. Mech. Phys. Solids 61 (4) (2013) 1091–1105.

[8] T. Bieler, P. Eisenlohr, F. Roters, D. Kumar, D. Mason, M. Crimp, D. Raabe, The role of heterogeneous deformation on damage nucleation at grain boundaries in single phase metals, Int. J. Plast. 25 (9) (2009) 1655–1683. Exploring new horizons of metal forming research.

[9] L. Kachanov, Introduction to Continuum Damage Mechanics. Vol. 10, Springer Science & Business Media, 1986.

[10] J. Chaboche, Continuum damage mechanics 1. General concepts, Trans. ASME, J. Appl. Mech. 55 (1) (1988) 59–64.

[11] M. Šilhavý, The Mechanics and Thermodynamics of Continuous Media, Springer, 1997.

[12] B. Svendsen, On the thermodynamic- and variational-based formulation of models for inelastic continua with internal lengthscales, Comput. Methods Appl. Mech. Engrg. 48 (2004) 5429–5452.

[13] B. Svendsen, S. Bargmann, On the continuum thermodynamic rate variational formulation of models for extended crystal plasticity at large deformation, J. Mech. Phys. Solids 58 (2010) 1253–1271.

[14] S. Forest, Micromorphic approach for gradient elasticity, viscoplasticity, and damage, J. Eng. Mech. 135 (3) (2009) 117–131.

[15] R. Peerlings, M. Geers, R. de Borst, W. Brekelmans, A critical comparison of nonlocal and gradient-enhanced softening continua, Int. J. Solids Struct. 38 (44–45) (2001) 7723–7746.

[16] K. Pham, H. Amor, J.-J. Marigo, C. Maurini, Gradient damage models and their use to approximate brittle fracture, Int. J. Damage Mech. 20 (4, SI) (2011) 618–652.

[17] B. Bourdin, G.A. Francfort, J.J. Marigo, Numerical experiments in revisited brittle fracture, J. Mech. Phys. Solids 48 (2000) 797–826.

[18] C. Miehe, F. Welschinger, M. Hofacker, Thermodynamically consistent phase field models for fracture: variational principles and multi-field FE implementations, Internat. J. Numer. Methods Engrg. 83 (2010) 1273–1311.

[19] C. Kuhn, R. Müller, A continuum phase field model for fracture, Eng. Fract. Mech. 77 (2010) 3625–3634.

[20] R. Spatschek, E. Brener, A. Karma, Phase field modeling of crack propagation, Phil. Mag. 91 (1) (2011) 75–95.

[21] M.J. Borden, C.V. Verhoosel, M.A. Scott, T.J. Hughes, C.M. Landis, A phase-field description of dynamic brittle fracture, Comput. Methods Appl. Mech. Engrg. 217 (2012) 77–95.

[22] M. Ambati, T. Gerasimov, L. De Lorenzis, A review on phase-field models of brittle fracture and a new fast hybrid formulation, Comput. Mech. 55 (2) (2015) 383–405.

[23] Y. Wang, J. Li, Phase field modeling of defects and deformation, Acta Mater. 58 (4) (2010) 1212–1235.

[24] B. Bourdin, G.A. Francfort, J.-J. Marigo, The variational approach to fracture, J. Elasticity 91 (1–3) (2008) 5–148.

[25] G. Del Piero, A variational approach to fracture and other inelastic phenomena, J. Elasticity 112 (1) (2013) 3–77.

[26] C. Miehe, M. Hofacker, L.-M. Schänzel, F. Aldakheel, Phase field modeling of fracture in multi-physics problems. Part II. Coupled brittle-to-ductile failure criteria and crack propagation in thermo-elastic–plastic solids, Comput. Methods Appl. Mech. Engrg. 294 (2015) 486–522.

[27] J.W. Cahn, J.E. Hilliard, Free energy of a nonuniform system. i. Interfacial free energy, J. Chem. Phys. 28 (2) (1958) 258–267.

[28] S.J. Benson, T.S. Munson, Flexible complementarity solvers for large-scale applications, Optim. Methods Softw. 21 (1) (2006) 155–168.

[29] F. Roters, P. Eisenlohr, L. Hantcherli, D. Tjahjanto, T. Bieler, D. Raabe, Overview of constitutive laws, kinematics, homogenization and multiscale methods in crystal plasticity finite-element modeling: Theory, experiments, applications, Acta Mater. 58 (4) (2010) 1152–1211.

[30] D. Peirce, R. Asaro, A. Needleman, Material rate dependence and localized deformation in crystalline solids, Acta Metall. 31 (12) (1983) 1951–1976.

[31] F. Roters, P. Eisenlohr, C. Kords, D. Tjahjanto, M. Diehl, D. Raabe, Damask: the duesseldorf advanced material simulation kit for studying crystal plasticity using an FE based or a spectral numerical solver. Procedia IUTAM 3, 3–10, IUTAM Symposium on Linking Scales in Computations: From Microstructure to Macro-scale Properties, 2012.

[32] S. Balay, S. Abhyankar, M.F. Adams, J. Brown, P. Brune, K. Buschelman, L. Dalcin, V. Eijkhout, W.D. Gropp, D. Kaushik, M.G. Knepley, L.C. McInnes, K. Rupp, B.F. Smith, S. Zampini, H. Zhang, PETSc users manual (ANL-95/11 - Revision 3.6), 2015.

[33] S.C. Eisenstat, H.F. Walker, S.C. Eisenstatt, Homer, F. Walker, Choosing the forcing terms in an inexact Newton method, SIAM J. Sci. Comput. 17 (1994) 16–32.

[34] Y. Saad, A flexible inner-outer preconditioned gmres algorithm, SIAM J. Sci. Comput. 14 (2) (1993) 461–469.

[35] P. Vaněk, J. Mandel, M. Brezina, Algebraic multigrid by smoothed aggregation for second and fourth order elliptic problems, Computing 56 (3) (1996) 179–196.

[36] B. Bourdin, Numerical implementation of the variational formulation for quasi-static brittle fracture, Interfaces Free Bound. 9 (3) (2007) 411–430.

[37] H. Amor, J.-J. Marigo, C. Maurini, Regularized formulation of the variational brittle fracture with unilateral contact: Numerical experiments, J. Mech. Phys. Solids 57 (8) (2009) 1209–1229.